

A Computational-Intelligence-Based Approach for Detection of Exudates in Diabetic Retinopathy Images

Alireza Osareh, Bitá Shadgar, and Richard Markham

Abstract—Currently, there is an increasing interest for setting up medical systems that can screen a large number of people for sight threatening diseases, such as diabetic retinopathy. This paper presents a method for automated identification of exudate pathologies in retinopathy images based on computational intelligence techniques. The color retinal images are segmented using fuzzy c-means clustering following some preprocessing steps, i.e., color normalization and contrast enhancement. The entire segmented images establish a dataset of regions. To classify these segmented regions into exudates and nonexudates, a set of initial features such as color, size, edge strength, and texture are extracted. A genetic-based algorithm is used to rank the features and identify the subset that gives the best classification results. The selected feature vectors are then classified using a multilayer neural network classifier. The algorithm was implemented using a large image dataset consisting of 300 manually labeled retinal images, and could identify affected retinal images with 96.0% sensitivity while it recognized 94.6% of the normal images, i.e., the specificity. Moreover, the proposed scheme illustrated an accuracy including 93.5% sensitivity and 92.1% predictivity for identification of retinal exudates at the pixel level.

Index Terms—Fuzzy c-means (FCMs), Gabor filters, genetic algorithms (GAs), neural networks, retinal exudates, thresholding.

I. INTRODUCTION

DIABETIC retinopathy (DR) is one of the most serious complications of diabetes and a major cause of visual morbidity. It is a progressive disease classified according to the presence of various clinical abnormalities. DR is the most common cause of blindness in people aged 30–69 years [1]. One-fifth of patients with newly discovered type II diabetes have retinopathy at the time of diagnosis. In type I diabetes, vision threatening retinopathy almost never occurs in the first five years after diagnosis or before puberty. After 15 years, however, almost all patients with type I and two-thirds of those with type II diabetes have background retinopathy [1].

DR is usually asymptomatic until the disease is at a late stage, making early detection and treatment essential. Thus, there is an increasing attention for setting up medical systems that can screen a large number of people to diagnose the DR

early enough for an optimal treatment. These systems should detect early signs of retinopathy and provide objective diagnosis based on criteria defined by ophthalmologists. To build such automated systems, different components are needed for recognizing retinal anatomical features, i.e., optic disc, fovea, blood vessels, and certain pathologies, such as exudates, hemorrhages, and microaneurysms.

In nonproliferative retinopathy [2], damaged retinal vessels leaked fatty and protein-based particles referred to as exudates. Intraretinal fatty (hard) exudates are a visible sign of DR and also a marker for the presence of coexistent retinal edema. If accumulate in the central part of the retina (macular area), edema and exudates are a major cause of visual loss in the nonproliferative forms of DR [3]. Exudates are associated with patches of vascular damage with leakage and typically manifested as spatially random yellow-white patches of varying sizes and shapes.

Here, we have concentrated on detecting exudates as the prime marker of DR disease because exudates are directly related to retinal edema and visual loss, and they are the single most important retinal lesion detectable in retinal images. On the other hand, detecting retinal exudates in a large number of images that are generated by screening programmes and need to be repeated at least annually is very expensive in professional time and open to human error.

With this motivation in mind, we have developed an efficient system to automate the preliminary analysis and diagnosis of DR disease. This system combines computational intelligence and pattern recognition with machine learning techniques to analyze diabetic retinal images. Through this system, the abnormal retinal images are automatically discriminated from normal images, and an accurate assessment of retinopathy severity is obtained at pixel level.

II. BACKGROUND

Few investigations in the past have identified retinal exudates from retinal images [4]–[12]. Here, to compare these methods against our proposed approach, we introduce two main criteria, i.e., lesion-based and image-based, for assessing the diagnostic accuracy of an exudate detection technique. In the lesion-based criterion, each single exudate lesion is regarded as an individual connected region, where this region can comprise one or more pixels. Each abnormal retinal image can be segmented into a number of exudate regions. By considering a set of retinal images and applying an appropriate segmentation technique, a dataset of exudate regions will be created.

Manuscript received November 26, 2007; revised May 21, 2008 and September 15, 2008. Current version published July 6, 2009.

A. Osareh and B. Shadgar are with the Computer Science Department, Engineering Faculty, Shahid Chamran University, Ahvaz 61357-83151, Iran (e-mail: alireza.osareh@scu.ac.ir; bita.shadgar@scu.ac.ir).

R. Markham is with Bristol Eye Hospital, Bristol BS1 2LX, U.K. (e-mail: richard.markham@ubht.nhs.uk).

Color versions of one or more of the figures in this paper are available online at <http://ieeexplore.ieee.org>.

Digital Object Identifier 10.1109/TITB.2008.2007493

Then, the lesion-based accuracy can be measured in terms of lesions sensitivity and specificity by comparing the obtained results against ophthalmologist's outline of the exudates. However, it is not the number of exudates that is important for the diagnosis. If an algorithm can find all exudates, but not the borders in a correct manner, it shows good statistics but poor performance.

In fact, the lesion-based accuracy can be assessed either in a pixel-level (pixel resolution) basis or alternatively using a larger collection of pixels, e.g., 10×10 patches (patch resolution). Although creating an accurate pixel-based ground truth is not an easy task, but a pixel resolution measure will be more precise than the patch resolution counterpart. In fact, a patch may only be partially covered by exudate pixels. Thus, the effects of misclassification errors for individual patches should be taken into consideration when the performance is not measured based on pixel resolution.

Alternatively, in an image-based diagnostic assessment way, the objective is to provide a logical predicate of the condition of the undertaken image. In this case, each image is examined and a decision is made to illustrate whether the image has some evidence of DR, purely based on the absence or presence of exudates anywhere in the image. Hence, the system's global image-based accuracy can be measured using a proportion of the tested normal–abnormal images to the number of images, which are correctly identified.

Exudates detection and identification was investigated by Phillips *et al.* [4], [5]. Global and local thresholding values were used to segment exudate lesions. Before thresholding, the images were preprocessed to eliminate photographic nonuniformities, and the contrast of the exudates was then enhanced. The lesion-based sensitivity of this technique was reported between 61% and 100% [5] based on 14 images. This paper did not provide any image-based accuracy. A drawback of this method was that other bright lesions (such as cotton wool spots) could be identified mistakenly.

Ege *et al.* [6] located exudates and cotton wool spots in 38 color images. These abnormalities were initially detected using a combination of template matching, region growing, and thresholding techniques. During the first stage, 87% of exudates were detected while detection rate for the cotton wool spots was up to 95% in terms of lesion-based criterion. Then, a Bayesian classifier was engaged to classify the bright lesions into exudates, cotton wool spots, and noise. The classification performance for this stage was only 62% for exudates and 52% for the cotton wool spots.

Wang *et al.* [7] addressed the same problem by using a minimum-distance discriminant classifier to identify the retinal bright lesions such as exudates and cotton wool spots. The spherical color space was chosen to represent the color features. Because in this study, the objective was to identify bright lesions, cotton wool spots, were also incorrectly classified as exudates. The image-based diagnostic accuracy of this approach was reported as 100% sensitivity and 70% specificity based on a dataset of 150 images.

In addition to the discussed techniques, neural networks (NNs) have also been exploited to classify the retinal exudates.

After median smoothing, the green channels of photographed images were fed directly into a very large NN (using 20×20 patches, with 400 inputs) in [8]. The NN was trained for five days and the lesion-based sensitivity of the exudate detection method was 93.1%. This performance was the result of classifying the whole 20×20 pixel patches rather than a pixel resolution classification.

Another NN-based exudate detection work was conducted by Hunter *et al.* [9]. The NN was trained to distinguish exudates from drusen based on 16×16 pixel patches. The authors introduced a hierarchical feature selection method, based on sensitivity analysis to distinguish the most relevant features. The final NN architecture had 11 input variables and achieved 91% lesion-based (patch resolution) performance using 15 retinal images. The reported performance was based on whether each 16×16 pixel patch contains exudates, and no image-based and pixel-level validation was reported.

Sinthanayothin [10] applied a recursive region growing technique using selected threshold values in gray-level images. In this paper, it was supposed that the processed retinal images are only including exudates, and other bright lesions were not considered. The author reported a lesion-based accuracy of 88.5% sensitivity and 99.7% specificity for the detection of exudates against a small dataset comprising 21 abnormal and 9 normal retinal images. However, these performances were measured based on 10×10 patches.

Walter *et al.* [11] identified exudates from green channel of the retinal images according to their gray-level variation. After initial localization, the exudates contours were subsequently determined by mathematical morphology techniques. This approach had three parameters: the size of the local window, which was used for calculation of the pixel local variation, and two other threshold values. The first threshold determines the minimum variation value within each local window. The candidate exudate regions were initially found based on the first threshold value. The second threshold represents the minimum value, by which a candidate must differ from its surrounding background pixels to be classified as exudates. This technique achieved a pixel resolution accuracy including 92.8% mean sensitivity and 92.4% mean predictivity against a set of 15 abnormal retinal images. The authors, however, ignored some types of errors on the border of the segmented exudates in their reported performances. In fact, when a pixel was not selected by the clinician as exudate but it was wrongly chosen by the algorithm, if the pixel was next to a selected exudate pixel by the clinician, it was not considered as a false positive (FP). A set of 15 normal retinal images was also examined, where in 13 of these images, no exudates were found (88.6% specificity in terms of image-based accuracy). This algorithm also did not discriminate exudates from cotton wool spots.

Niemeijer *et al.* [12] distinguished the bright lesions, i.e., exudates, cotton wool spots, and drusen from color retinal images. In the first step, the image pixels were classified, resulting in a lesion probability map that indicated the probability of each pixel to be part of a bright lesion. Then, pixels with high probability were grouped into probable lesion pixel clusters. In the next step, based on cluster characteristics, each probable cluster was

assigned a probability indicating the likelihood that the cluster was a true bright lesion. Finally, these clusters were classified as exudate, cotton wool spot, or drusen. The author reported a pixel resolution accuracy of 95.5%, 70.0%, and 77.0% sensitivity, and 86.0%, 93.0%, and 88.0% specificity for the detection of exudates, cotton wool spots, and drusen, respectively, against a set of 300 retinal images.

Simple thresholding techniques are unlikely to present consistent results for identification of exudates against a large dataset of retinal images. Although most exudates show higher gray-level values compared to the nearby retinal background, some smaller ones have about the same intensity as the background of the retinal. Hence, due to significant gray-level changes in the whole image and between the images, it is difficult to find a global threshold.

As is apparent, past works on exudates identification mainly relied on gray-level information, and were not evaluated on large datasets or failed to give good results for large numbers of images as encountered in a screening process. Moreover, the majority of these methods were assessed only in terms of either lesion-based [4]–[6], [8]–[10] or image-based [7] criterion. Indeed, the reported lesion-based accuracies were often based on 10×10 or 20×20 patches (patch resolution) [8]–[10], and no pixel resolution validation was accomplished except in a couple of works [11], [12]. There were clearly certain errors in reported patch resolution accuracies due to the small areas, which some exudates could occupy. However, in medical decision support systems such as ours, an accurate diagnostic accuracy assessment in terms of both pixel resolution and image-based is important.

Although high-resolution color cameras are the accepted standard for screening programmes, automated diagnosis systems generally tend to base their analysis on intensity information alone, either from red-free images [4], [5] or using the green channel of red, green, blue (RGB) color images [6], [8]–[12].

More than a decade ago, Goldbaum *et al.* [13] have discriminated similarly colored objects in retinal images based on color information. Since then, not many works have shown interest in color classification of retinal images. In fact, using retinal color information has its own challenges. For example, without some type of color normalization for the background pigmentation, the large variation in natural retinal pigmentation across the population confounds discrimination of the relatively small variations between the different lesion types. In our opinion, using color information in conjunction with other features, such as size, shape, and texture, leads to better exudate discrimination ability. Thus, we take advantage of retinal color information toward our objectives and show the improvement obtained over gray-level-based techniques.

Computational intelligence has emerged as a rapidly growing field in recent years. Its various techniques, e.g., NNs, fuzzy systems, evolutionary computing, and machine learning have been recognized as a collection of powerful tools for intelligent information processing, decision making, and knowledge management in applications such as medical diagnosis. This could be due to the potential of these systems to deal in a suitable way with imprecision, uncertainty, and partial truth.

Here, we aim to investigate the effectiveness of computational intelligence toward automatic detection and identification of exudate pathologies. In this way, we have constructed a large dataset of 300 manually labeled images for an accurate training and evaluation of our method. Following a color normalization and contrast-enhancement preprocessing steps, the retinal images are segmented based on a combination of color representation in *Luv* color space and an efficient coarse to fine segmentation using fuzzy c-means (FCM) clustering. Genetic algorithms (GAs) are exploited to select the most appropriate features from the segmented regions, and to classify these regions into exudates and nonexudates, an NN classifier is investigated. Finally, the diagnostic accuracy of the proposed method is evaluated in terms of both pixel resolution and image-based criteria against the manually labeled images.

III. MATERIALS AND METHODS

A. Image Acquisition

Here, we have constructed a large dataset of manually labeled images for both training and testing of our method. This dataset consists of 300 images taken from a screening program for DR in Bristol Eye Hospital. The images were acquired using a Cannon nonmydriatic CR6-45NM camera. Each image was captured using 24 bit per pixel at a resolution of 760×570 pixels [14]. Of the 300 images in the dataset, 150 are of patients with no pathologies (normal) and the rest of the images are abnormal (contain pathologies such as exudates, cotton wool spots, microaneurysms, and hemorrhages). Examples of such images are shown in Fig. 1. As can be seen, a normal image [Fig. 1(g) and (h)] mainly consists of blood vessels, optic disc, fovea, and the background, but the abnormal image also has multiple artifacts caused by DR disease [Fig. 1(a) and (b)].

B. Preprocessing

Typically, there is wide variation in the color of fundus from different patients that is strongly correlated to the person's race and iris color. Therefore, we put our data through two preprocessing steps before commencing the detection of exudates. The first step is to normalize the color of the retinal images across the dataset. We selected a retinal image as a reference [Fig. 2(a)], and then applied histogram specification [15] to modify the values of each image in the database [for example, Fig. 2(b)] such that its frequency histogram matched the reference image distribution. Fig. 2(c) shows the result of this normalization.

The histogram specification technique was independently applied to each individual RGB channel to match the shapes of three specific histograms of the reference image. Here, the reference histograms were taken from an image, which represents a frequent retinal pigmentation color among our image dataset. This image was chosen in agreement with the expert ophthalmologist.

The contrast of retinal images was not sufficient due to the intrinsic attributes of lesions and decreasing color saturation, especially in the periphery. Consequently, in the second

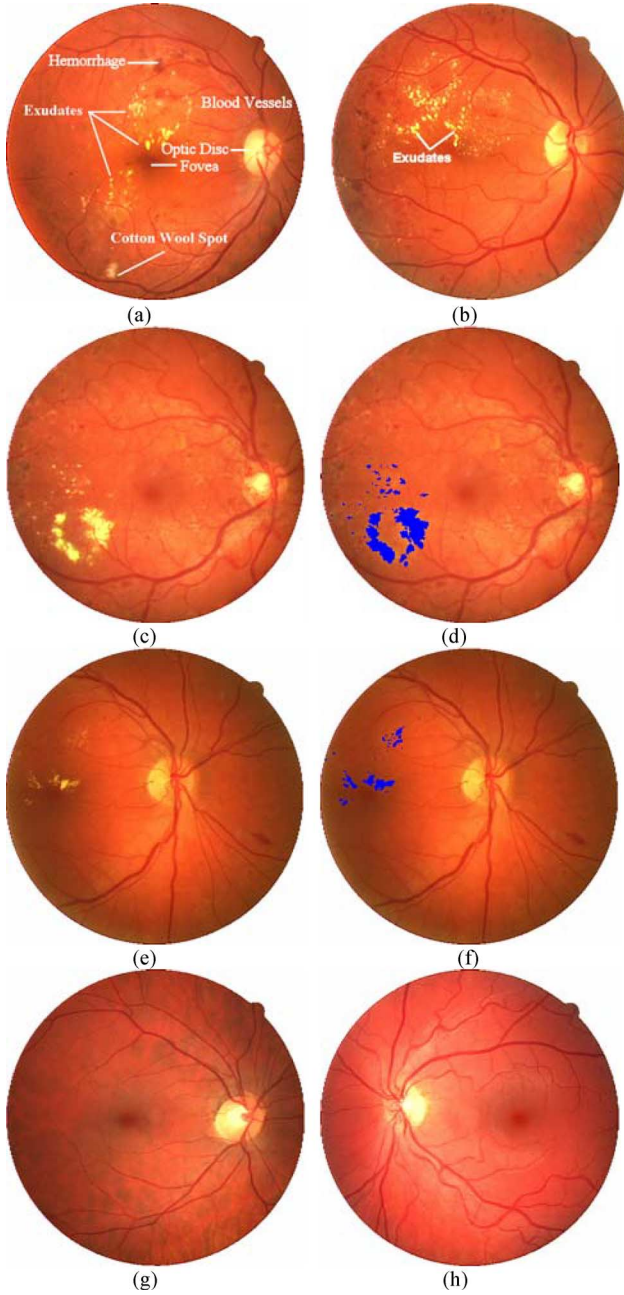


Fig. 1. Typical abnormal and normal images. (a) Abnormal image from our dataset indicates hemorrhage, exudates, blood vessels, optic disc, fovea, and cotton wool spot components. (b) Another image with exudate pathologies. (c) Typical abnormal image. (d) Manually segmented exudates. (e) Another abnormal image. (f) Manually segmented exudates. (g) Typical normal image. (h) Another typical normal retinal image.

preprocessing step, the contrast between the exudates and the retina background was enhanced to facilitate later segmentation. We applied local contrast enhancement [10] to distribute the values of pixels around the local mean. In this way, a pixel p in the center of a small running window w was changed to a new value p_n

$$p_n = 255 * \left(\frac{[\phi_w(p) - \phi_w(\text{Min})]}{[\phi_w(\text{Max}) - \phi_w(\text{Min})]} \right) \quad (1)$$

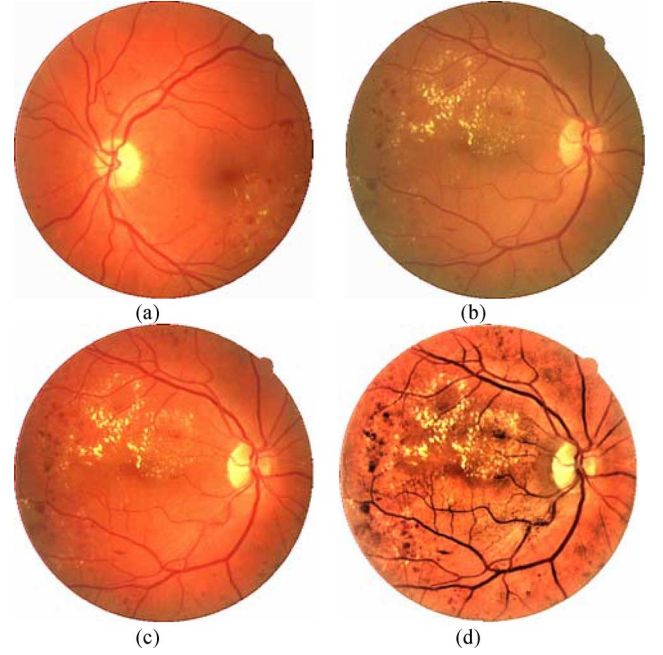


Fig. 2. Color normalization and contrast enhancement results. (a) Reference image. (b) Typical abnormal image. (c) Color normalized version of (b). (d) Contrast enhancement.

where

$$\phi_w(p) = \left[1 + \exp \left(\frac{\mu_w - p}{\sigma_w} \right) \right]^{-1} \quad (2)$$

and Max and Min are the maximum and minimum values in the whole image, while μ_w and σ_w indicate the local window mean and standard deviation, respectively. The exponential produces significant enhancement when the contrast is low (small σ_w), while it provides little enhancement if the contrast is high (large σ_w).

Fig. 2(d) shows the result of local contrast enhancement. While the contrast enhancement improves the contrast of exudate lesions, it may also enhance the contrast of some nonexudate background pixels (e.g., noise), so that these pixels can wrongly be identified as exudate lesions. Here, prior to contrast enhancement, a 3×3 median filter was applied to suppress the noise.

C. Retinal Image Segmentation Based on FCMs

There are general segmentation techniques that are functional for a variety of data. However, specific methods for particular applications can often achieve better performance by taking into account prior knowledge. Here, investigations are made to identify a robust method to reliably segment the retinal images. Hard segmentation methods make crisp decisions about regions. However, the regions in an image are not always crisply defined. On the other hand, fuzzy approaches provide a mechanism to represent and manipulate uncertainty and ambiguity, and allow pixels to belong to multiple classes with varying degrees of membership.

In this paper, we segment retinal images using a two-stage color segmentation algorithm based on Gaussian-smoothed histogram analysis and FCMs clustering [16].

The first task in color image processing is to choose an appropriate representation using a color space definition. In a suitable color space, color pixels of interest can be clustered into well-defined, less overlapping groups, which are easily bounded by segmentation algorithms in the color space.

Here, to select the most appropriate color space, we conduct a quantitative analysis and utilize the evaluation function value $R = \text{trace}(S_b/S_w)$ as a measure of color space efficiency [17]. This function estimates the class separability of our exudate and nonexudate pixel classes in different color spaces, and is measured in terms of between-class (S_b) and within-class (S_w) scatter matrices. The between-class scatter matrix represents the scatter of sample pixels around the mean vector of the class mixture, whereas the within-class criterion indicates the distribution of sample pixels around their respective mean vectors. In fact, the numerator of function R represents the overall color difference of exudate and nonexudate sample points, while the denominator denotes the variations of the color distribution for these two classes. A higher value of R shows that the classes are more separated, while the members within each class are closer to each other. We have experimented with various color spaces such as RGB, YIQ, HIS (hue, saturation, intensity), HSL (hue, saturation, lightness), Lab, and found *Luv* [18] color space the most appropriate space for our segmentation.

1) *Retinal Image Coarse Segmentation*: At the coarse stage, the segmentation algorithm utilizes the histogram information of the three 1-D color components to estimate the number of valid classes by a statistical evaluation of the histograms. It has been identified [19] that the derivatives, the extrema, and the interval bounded by the extrema of a histogram are useful information when carrying out a qualitative analysis of the histograms.

Witkin [19] proposed an approach based on multiscale representation of a measured signal, and used the Gaussian function to smooth the curve and detected the peaks and valleys using the structure of the two first-derivative extrema. Suppose we have a signal (histogram) f and a smoothing kernel $g(x, \sigma)$, then the smoothed signal at the scale σ can be written as

$$F(x, \sigma) = f(x) * g(x, \sigma) \quad (3)$$

where $*$ denotes convolution. F defines a surface in the (x, σ) plane, which is swept out as the Gaussian standard deviation is varied. Having smoothed the image's histograms based on a Gaussian smoothing, the coarse stage begins to segment the image using the located thresholds. The histogram valley locations can be possible solutions for the thresholds. The valleys are obtained by computing the first and second derivative of each 1-D histogram, and find the locations that satisfy the following equation:

$$F_x(x, \sigma) = f(x) * \frac{\partial g(x, \sigma)}{\partial x} = 0, \quad F_{xx}(x, \sigma) > 0. \quad (4)$$

The histogram peaks represent the number of clusters, and are localized as follows:

$$F_x(x, \sigma) = f(x) * \frac{\partial g(x, \sigma)}{\partial x} = 0, \quad F_{xx}(x, \sigma) < 0. \quad (5)$$

A zero crossing in F_x denotes a local maximum (peak) of $F(x)$ if its sign changes from plus to minus (when the F_{xx} is negative) and a local minimum (valley) if its sign changes from minus to plus (when the F_{xx} is positive). The aim of this manipulation is to obtain a set histogram thresholds that precisely cluster the colours, which emerge in the input image. Each of these clusters is separated from its neighbours by a secure-zone parameter as follows:

$$\begin{aligned} T_Low(i) &= \text{Peak}(i) * \text{Secure-zone} \\ &\quad + (1 - \text{Secure-zone}) * \text{Valley}(i - 1) \\ T_High(i) &= \text{Peak}(i) * \text{Secure-zone} \\ &\quad + (1 - \text{Secure-zone}) * \text{Valley}(i) \\ i &= 1, \dots, n. \end{aligned} \quad (6)$$

Here, T_Low and T_High are the cluster's lower and higher thresholds, Peak and Valley refer to the peak and valley locations in the histogram, and n is the number of preclusters (classes) that exist in the histogram. The histogram regions, which are bounded by a pair of thresholds, are considered as ambiguous regions. These regions will be further processed in the fine segmentation stage. By changing the secure-zone value (assumed to be between 0 and 1), which is a configurable parameter of the segmentation algorithm, we can readily adjust the peaks' overlapping extent, and thus the number of the image pixels, which are allocated to the ambiguous regions.

By projecting each color image onto its three color components (L , u , and v), one can obtain the number of peaks in each colour component, i.e., N_L , N_u , and N_v . The maximum number of possible 3-D peaks is then calculated as follows:

$$N_{\max} = N_L N_u N_v. \quad (7)$$

Thus, we can partition the *Luv* space into several hexahedra obtained as Cartesian products of peak intervals found for each color component. This can be stated as

$$\begin{aligned} \text{Cluster}(n) &= \sum_{L=T_Low(L_i)}^{T_High(L_i)} L(x, y) \wedge \sum_{u=T_Low(u_i)}^{T_High(u_i)} u(x, y) \\ &\quad \wedge \sum_{v=T_Low(v_i)}^{T_High(v_i)} v(x, y) \end{aligned} \quad (8)$$

where n is an index for hexahedral partitioned clustered (i.e., $n = 1, \dots, N_{\max}$), L , u , and v are the image's color components, and \wedge is a logical AND operator.

Therefore, the number of valid clusters and their corresponding mean vectors that are then utilized in the fine stage can be obtained. These pixels, which are not assigned to any valid clusters, are entered into ambiguous regions, and their fine segmentation is achieved within FCM clustering.

2) *Fine Segmentation Based on FCM Clustering*: In the fine stage, FCM assigns any remaining unclassified pixels (pixels from ambiguous regions) to the closest cluster based on a weighted similarity measure between the pixels in the image and each of C (e.g., exudates and nonexudates) cluster

centers [20]. Local extrema of this objective function are indicative of an optimal clustering of the image. The function is defined as

$$J_{\text{FCM}}(U, v; X) = \sum_{k=1}^n \sum_{i=1}^C (\mu_{ik})^m \|x_k - v_i\|^2, \quad 1 \leq m < \infty \quad (9)$$

where μ_{ik} is the fuzzy membership value of a pixel k to class i and $X = x_1, \dots, x_n$ is a finite dataset in R^d . $\{v = v_1, \dots, v_c\}$ is a set of class centers, where $v_i \in R^d$, $1 \leq i \leq C$, represents a d -dimensional i th class center, and is regarded as a prototype.

The objective function (9) is minimized when high membership values are assigned to pixels whose values are close to the centroid for its particular class, and low membership values are assigned when the pixel data are far from the centroid. Taking the first derivatives of (9) with respect to μ_{ik} and v_i , and setting them to zero yields necessary conditions for minimizing the objective function. The parameter m is a weighting exponent that satisfies $m > 1$ and controls the degree of fuzziness in the resulting membership functions. As m increases, the membership functions become increasingly fuzzy. In this paper, the value of m was assumed to be equal to 2, and the norm operator represented the standard Euclidean distance. For $m > 1$, local minimum can be defined using the following equations:

$$\begin{aligned} \mu_{ik} &= \frac{1}{\sum_{j=1}^C (\|x_k - v_i\| / \|x_k - v_j\|)^{2/(m-1)}} \quad \forall i, k, \\ v_i &= \frac{\sum_{k=1}^n (\mu_{ik})^m x_k}{\sum_{k=1}^n (\mu_{ik})^m} \end{aligned} \quad (10)$$

where the positive-definite matrix U is the fuzzy C partition of the input image pixels over the set of C cluster centers treated as vectors and v_i represents the i th class center. An important parameter in an FCM clustering algorithm is the number of classes (C) and their corresponding centers that are computed within the coarse segmentation stage. Hence, in this paper, there is no need to recompute the class centers v_i for exudate and nonexudate classes by using (10), and instead they are considered as sufficiently well approximated within the coarse segmentation phase. At this stage, pixels from ambiguous regions are assigned to the remaining clusters. Thus, for any unclassified pixel x with the feature vector x_k , the fuzzy membership function μ_{ik} is computed, which evaluates the degree of membership of the given pixel to the given fuzzy class v_i , $i = 1, \dots, C$. The resulting fuzzy segmentation is converted to a hard segmentation by assigning each pixel solely to the class that has the highest membership value for that pixel. As most pixels are classified in the coarse stage, a significant computation time required for FCM is saved.

D. Feature Selection Based on GAs

Once our color retinal images are segmented, each image is represented by its corresponding segmented regions. These regions, however, need to be identified in terms of exudates and nonexudates. This is attempted, in a bottom-up approach, by extracting a set of features for each region and classifying the regions based on the generated feature vectors.

To select a suitable set of features, it is necessary to take advantage of any prior knowledge of exudates and identify the characteristics that make them distinctive. Clinically, ophthalmologists use color to differentiate between various pathological conditions. We also consider region color as one of our main features. Similarly colored objects like exudates and cotton wool spots are differentiated with further features, such as size, edge strength, and texture.

Gabor filters are powerful tools that have been widely used as a model of texture for image interpretation tasks. Daugman [21] has utilized Gabor filters in an automatic system for verifying a person's identity using images of the iris. Jain *et al.* [22] have employed Gabor filters to perform segmentation of objects from complex backgrounds. Many other researchers have investigated Gabor filters for performing texture segmentation [23], [24].

Mathematically, a 2-D Gabor function g is the product of a 2-D Gaussian and a complex exponential function. When the Gaussian part is symmetric, we obtain the following isotropic Gabor function [25]:

$$g_{\theta, \lambda, \sigma}(x, y) = \exp \left\{ -\frac{x^2 + y^2}{2\sigma^2} \right\} \exp \left\{ \frac{j\pi}{\lambda} (x \cos \theta + y \sin \theta) \right\}. \quad (11)$$

The parameter θ represents filter orientation, λ is the filter's wavelength that modifies the sensitivity to high/low frequencies, and σ characterizes the filter standard derivation and equivalently represents scale value. With this parameterization, the Gabor function does not scale uniformly when σ changes. Thus, it is preferable to use a new parameter $\gamma = \lambda\sigma^{-1}$ instead of λ , so that a change in σ corresponds to a true scale change in the Gabor function.

Here, to encode appearance of FCM-based segmented regions in terms of texture, and thus discriminate more accurately the exudate regions from other nonexudates, a Gabor filter bank is used. This bank contains 108 filters, 12 orientations (θ spanning from 0° up to 180° at steps of 15°), three wavelengths ($\gamma = 1.5, 2.5, 3.5$), and three scales ($\sigma = 3, 5, 7$). The wavelength and scale values are experimentally tuned according to our prior knowledge of retinal image characteristics. The response of such a filter bank to an input image is a set of filtered images.

As was discussed in a previous section, our FCM-based segmentation approach segment each input image, yielding a set of image regions. The use of regions enables higher level concepts such as compactness, size, etc., to be considered. In addition to these features, we take into consideration the responses of all Gabor filters (filtered images) for each segmented region. To do that, we take the mean responses across the region for each filter. This assigns a 108-element feature vector to each segmented region. An overview of the initially chosen feature vectors is given In Table I.

Ideally, the classification process shall be based on a small number of significant features that effectively characterize the input data. Thus, many features are initially defined, and it is not known beforehand which ones will give good classification results and which ones will not. As an exhaustive search over all possible combinations of input features is quite expensive, to identify the best subset, we utilize a genetic-based algorithm to

TABLE I
SET OF INITIAL FEATURES CONSIDERED TO DISCRIMINATE EXUDATE REGIONS
FROM OTHER SEGMENTED REGIONS

Feature	Description
1	Compactness of the region
2	Region size
3	Length of the perimeter of the region
4	Region edge strength
5-7	Mean Luv values inside the region
8-10	Mean Luv values outside the region
11-13	Standard Deviation of Luv values inside the region
14-16	Standard Deviation of Luv values outside the region
17-124	Region Mean Gabor filter responses

rank the features and identify the subset that will give the best classification results.

GA offers an attractive approach to multimodal optimization problems [26]. When applying these algorithms to a particular problem, there are three main points to be taken into account [27]: representation (coding) of the candidate solutions, objective function to be maximized, and genetic operators that are used and their probabilities of occurrence. In this paper, a binary coding representation is considered for the candidate solutions, and individuals (possible solutions) are represented by a binary vector of length 124. A standard GA with a rank-based selection strategy is used with a one-point crossover operator.

The evaluation function that measures the fitness of each solution is $p = 1/\text{EER}$, where EER is the equal error rate. Therefore, the objective of the GA is to find a solution among all possibilities that maximizes p . Here, the EER is measured according to the similarity scores calculated using the Mahalanobis distance [17].

E. Region Level Classification Using NNs

To classify the segmented regions, we exploit well-known NNs discriminative classifiers [28]. Having selected the optimum feature set based on GA, a corresponding 65-D feature vector [comprising feature numbers 1–2, 4–13, and 53 Gabor response features (Table I)] is computed for each segmented region. The multilayer perceptrons NN with three layers has a 65-node input layer corresponding to the feature vector. We experiment with hidden layers through a range of 2–20 hidden units to find the optimum architecture where all networks are trained using backpropagation learning method. A single output node gives the final classification probability, and the sigmoid activation functions are used in the hidden and output layers.

IV. RESULTS

A. Retinal Image Segmentation Results

To investigate the effectiveness of the proposed method, an image dataset of 300 labeled retinal images including 150 normal and 150 abnormal images is considered. To evaluate the efficiency of the proposed region-level classification scheme including image preprocessing, FCM-based segmentation, GA-based feature selection, and NN-based classification, 75 abnormal and 75 normal images from our image dataset are con-

TABLE II
COARSE SEGMENTATION RESULTS FOR THE IMAGE SHOWN IN FIG. 3(a)
WITH ($\sigma = 5$)

Initial Nonzero Classes	Number of Pixels	Class Mean Luv Values			Assigned Color
		L	u	v	
1	669	2.6	4.2	20.6	Green
2	214553	72.7	59.1	59.5	Orange
3	4081	97.8	5.2	65.7	Yellow

Number of image pixels = 227 560, unclassified pixels after coarse stage = 8257.

TABLE III
FINE SEGMENTATION RESULTS FOR THE IMAGE SHOWN IN FIG. 3(b)

Final Classes	Number of Pixels	Class Mean Luv Values		
		L	u	v
1	669+2865	18.5	27.9	30.6
2	214553+906	72.5	59.5	59.1
3	4081+4486	94.5	13.9	66.9

sidered. The remaining 150 images are utilized as unseen images to validate the effectiveness of our exudate recognition approach in terms of both image-based and pixel-resolution accuracies. We used the image shown in Fig. 2(d), which is a preprocessed retinal image as a running example to illustrate each stage of the method. The segmentation scheme begins by Gaussian filtering of Luv histograms of this image to derive the number of clusters and approximate the location of their centers. The segmentation algorithm requires two parameters, i.e., scale (σ) and secure-zone that need to be defined.

Scale parameter (σ) controls the smoothing extent of the histograms' fine structures. By reducing the value of this parameter, the histogram smoothing degree is decreased, and thus, the fine structures are less suppressed.

The secure-zone parameter has a direct effect in evaluating the lower and higher threshold values (6), and it thus influences the number of pixels, which are allocated to the ambiguous regions and passed to the fine segmentation stage.

Here, the optimum σ and secure-zone values are experimentally tuned ($\sigma = 5$, secure-zone = 0.4) according to our prior knowledge of retinal image characteristics and the conducted experiments of different values. Indeed, to not discard any true exudate pixels, we adjust these parameters in favor of more FPs than false negatives (FNs).

Table II summarizes the obtained measurements when the image in Fig. 2(d) is coarsely segmented. In this case, three valid classes are distinguished. These are related to the background, blood vessels/red lesions, and the exudates/cotton wool spots, respectively. From 227 560 pixels, the coarse stage assigns 669 pixels to the blood vessels/red lesions class, 214 553 pixels to the background class, and 4081 pixels to candidate exudates/cotton wool spots class. Another 8257 pixels (3.6% of all initial pixels) are left unclassified at this stage. This table also shows the mean Luv color values of each valid class and the subjective colors that are assigned to the classes.

Table III represents how the remaining unclassified pixels are assigned to the valid classes within the fine stage. In fact, 2865 unclassified pixels are classified as blood vessels/red lesions,

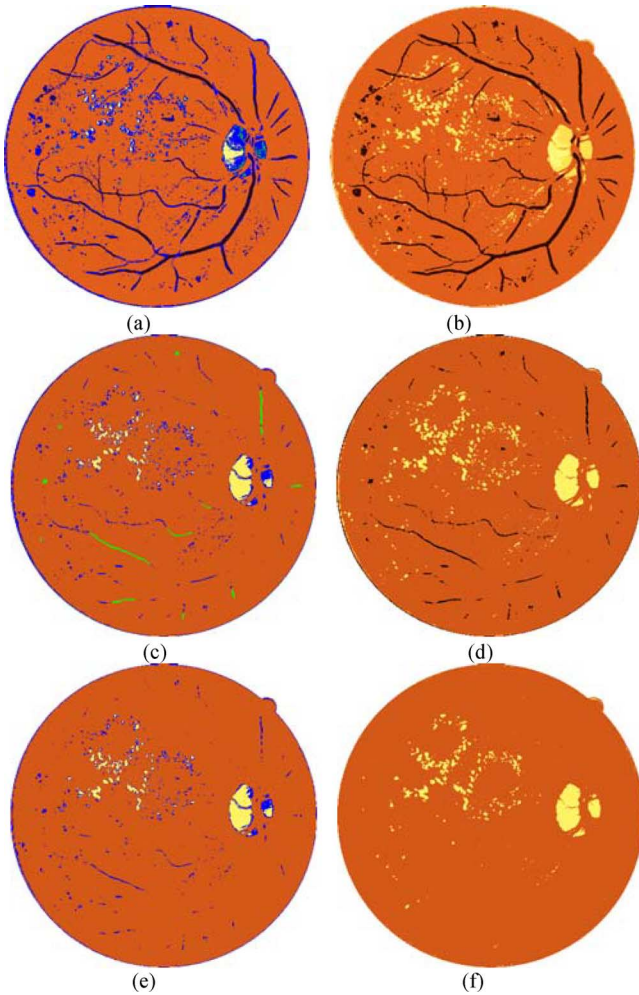


Fig. 3. Colour segmentation results. (a) Coarse segmentation result ($2\sigma = 3$) for image in Fig. 2(d). (b) Fine segmentation result ($\sigma = 3$). (c) Coarse segmentation result ($\sigma = 5$). (d) Fine segmentation result ($\sigma = 5$). (e) Coarse segmentation result ($\sigma = 7$). (f) Fine segmentation result ($\sigma = 7$).

906 pixels as background, and the remaining 4486 assigned to the exudates/cotton wool spots class.

Fig. 3(c) shows the coarse segmentation result for our running example retinal image. There are three final clusters, i.e., background (orange), blood vessels/red lesions (green), and exudates/cotton wool spots (yellow), in addition to the unclassified pixels, which are marked in blue. The final segmentation result is shown in Fig. 3(d). It is apparent that the actual exudates and some FPs, including optic disc regions, are included in the candidate exudates cluster. FP exudate regions arise because of other pale objects including retinal light reflections, cotton wool spots, and most significantly, the optic disc. The light reflection artifacts, mostly along large blood vessels are, an important source of FPs. These artifacts can be seen in Fig. 3(b). Thus, it is crucial to distinguish true exudates using a region-based classification scheme, but prior to that the FP optic disc regions are removed from the other segmented regions using our proposed automatic optic disc localization technique [29].

Similarly, Fig. 3(a) shows the coarse segmentation result with scale parameter σ equal to 3. In this case, the image was seg-

mented into four clusters, including background, blood vessels/red lesions, and exudates/cotton wool spots, which comprised two different clusters. The final segmented image is shown in Fig. 3(b). In this paper, we would prefer to segment the exudates into one representative cluster; otherwise, the following processing stages can be affected. Thus, it is required to exploit further methods, such as region merging, to cope with the over segmentation of the exudates.

In a reverse trend, it is expected that the segmentation results degenerate with higher value of σ than the selected optimum ($\sigma = 5$), as the smoothing extent is increased, and thus, the histograms' fine structures are more suppressed. Fig. 3(e) shows the coarse segmentation result with scale parameter σ equal to 7, where the image is segmented into two clusters, i.e., background and exudates/cotton wool spots. The final segmented image is shown in Fig. 3(f). However, as is apparent, in this case, some faint exudates are missed.

We also attempt a series of experiments to determine the *secure-zone* optimum value. It is observed that as this parameter enlarged, the histogram lower threshold value was also increased, while the higher threshold was decreased. Thus, the widths of the histogram's regions, which are bounded by a pair of lower and higher thresholds, are reduced. This, in turn, forces a higher number of pixels to remain in the ambiguous regions. It thus leads to a reduction in the number of image pixels, which are assigned to the valid classes within coarse stage. Having set the segmentation parameters, we apply the technique to all 150 images using $\sigma = 5$ and *secure-zone* = 0.4, respectively. This results in 9856 segmented regions. These regions are then labeled by an expert ophthalmologist as 7122 exudates and 2734 nonexudates. The segmented regions are divided into separate training, validation, and test sets. Among several NNs containing varying numbers of hidden units that are trained, a network, with 12 hidden units performs best in terms of the overall generalization ability. This classifier achieves an overall generalization accuracy of 95.3% with 94.9% sensitivity and 93.8% specificity in terms of regions classification.

So far, we have discussed the region-level classification of a set of segmented regions using NN classifiers. We can also use the trained classifiers to evaluate the effectiveness of our exudate recognition approach in terms of both introduced image-based and pixel-resolution accuracies. To do that, a population of 150 new retinal images is considered, including 75 abnormal and 75 normal images. Each new image is segmented and the measured feature vectors are evaluated using our optimum NN classifier. A final decision is then made as to whether the image has some evidence of retinopathy in terms of exudate lesions. The proposed system can identify affected retinal images with 96.0% sensitivity (correct classification of 72 abnormal images out of 75) while it recognizes 94.6% of the normal images, i.e., the specificity (correct classification of 71 normal images out of 75).

On the other hand, classification of the whole new 150 retinal image pixels in a pixel resolution basis is required to work on an imbalanced dataset of exudate and nonexudate pixels, where the number of TNs was much higher than FPs. Hence, the specificity criterion is mostly near 100% and do not represent an

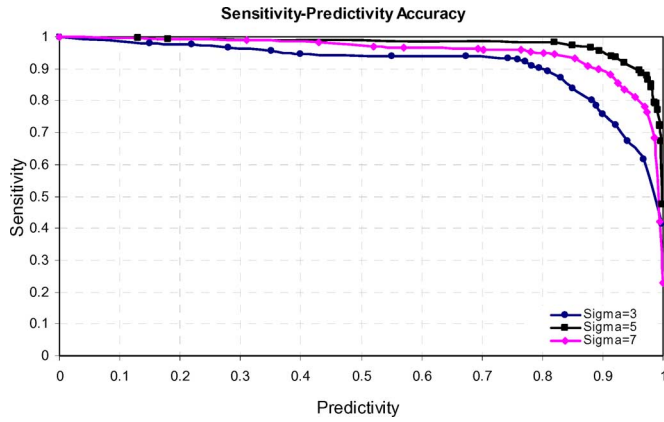


Fig. 4. Accuracy of proposed method in terms of sensitivity–predictivity criteria for three different σ values.

informative measurement. Thus, we use the predictivity measure instead. By changing the NN output threshold from 0 to 1, we can achieve different tradeoffs between sensitivity and predictivity criteria, and obtained various points in the receiver operating characteristic (ROC) space. This procedure is carried out for each individual image of the new set of retinal images. Then the average of all image's sensitivity and predictivity values is determined to get the final points in the ROC space (Fig. 4).

In order to investigate the influence of the segmentation's main parameter (σ) and validate the robustness of the algorithm, the ROC analysis is carried out for three different σ values, i.e., 3, 5, and 7. Fig. 4 shows the obtained ROC graphs. As is evident, the segmentation results with $\sigma = 5$ outperforms the other two examined σ values by achieving higher levels of diagnostic accuracy in terms of sensitivity–predictivity criteria over the whole ROC space. The highest overall performance is including 93.5% sensitivity and 92.1% predictivity. These results also provide a good balance between sensitivity and predictivity measurements. However, according to the requirements of the task, other specifications can be readily utilized. For example, by changing the NN output threshold value, the sensitivity is increased to 96.8% with a lower predictivity equal to 88%. We observe that the segmentation results get worst for $\sigma = 3$, but even in this case, we could achieve a sensitivity of 89.2% with 81% predictivity.

Fig. 5 shows the application of our exudate recognition method on three retinal images where the exudates were identified using our trained optimum NN classifier. From Fig. 5(b), (d), and (f), it is apparent that this approach can efficiently identify the retinal exudates. Due to the light reflection, there are, however, some high-intensity artifacts near large retinal blood vessels. These artifacts are one of the main sources of FP regions in the classified images. This can be clearly seen in Fig. 5(b), where these artifacts have created some segmented regions above and below the optic disc region. Although most of these falsely segmented regions are classified as nonexudates during the classification process, a few are wrongly assigned to the exudates class [Fig. 5(b)]. Another possible source of FP regions is cotton wool spots. We therefore include some descrip-

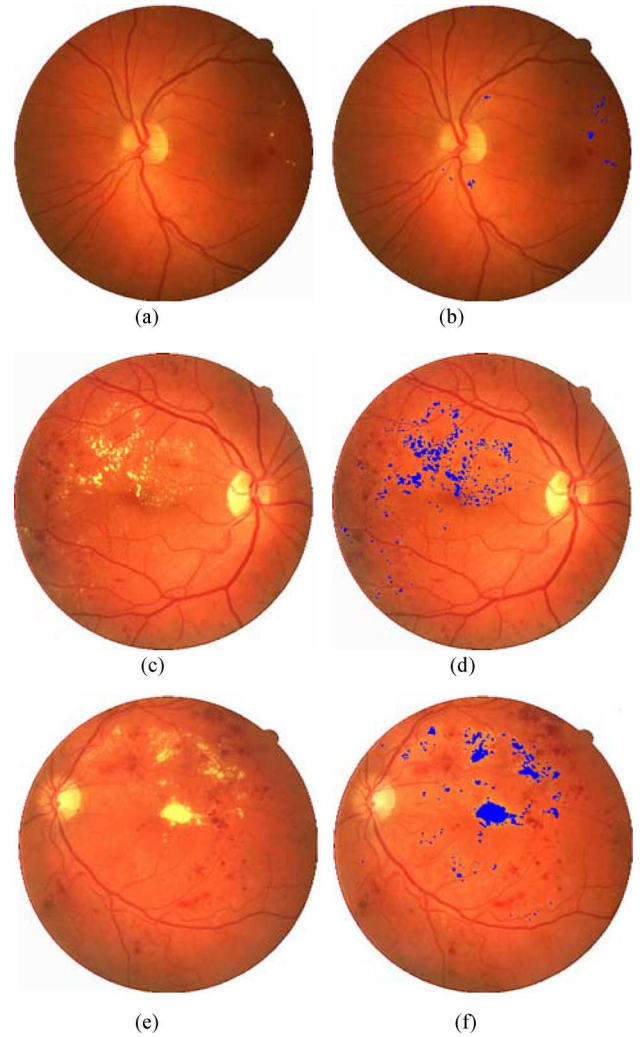


Fig. 5. Exudates identification results. (a) Typical abnormal retinal image. (b) NN-based identified exudates. (c) Another abnormal image. (d) NN-based identified exudates. (e) Abnormal image. (f) NN-based identified exudates.

tors such as edge strength and texture in our feature vectors to differentiate cotton wool spots from exudates.

According to our best knowledge, there is not yet any publicly available benchmark dataset comprising large number of manually segmented retinal images. Thus, a fair comparison of different segmentation results that are obtained using diverse retinal images is difficult. There is another difficulty in implementing other people's algorithms due to lack of necessary details. In this paper, to evaluate the diagnostic accuracy of our exudate identification technique, we define two necessary assessment criteria, i.e., image-based and lesion-based (patch-resolution or pixel-resolution) accuracies. These criteria enable us to measure both our proposed method accuracy and compare our results against the other works.

Here, we compare our results with the most related works in the literature. These are the works of Wang *et al.* [7], Gardner *et al.* [8], Sinthanayothin [10], Walter *et al.* [11], and Niemeijer *et al.* [12]. Table IV summarizes all the results in terms of both lesion-based and image-based diagnostic accuracies.

TABLE IV
LESION-BASED AND IMAGE-BASED COMPARISON OF OUR PROPOSED METHOD
AGAINST PREVIOUS TECHNIQUES

Identification Method	Lesion-Based		Image-Based	
	Sensitivity	Predictivity	Sensitivity	Specificity
Wang et al.	-	-	100.0	70.0
Gardner et al.	93.1 [*]	-	-	-
Sinthanayothin	88.5 [*]	99.7 ^{*§}	-	-
Niemeijer et al.	95.5 [†]	86.0 [§]	-	-
Walter et al.	92.8 [†]	92.4 [†]	100.0	88.6
Our Method	93.5 [†]	92.1 [†]	96.0	94.6

^{*}Denotes patch resolution.

[†]Refers to pixel resolution.

[§]Represents specificity (%).

Wang *et al.* [7] reported an image-based accuracy of 100.0% sensitivity and 70.0% specificity without any assessment in terms of lesion-based or pixel-resolution accuracies. The authors in [8] achieved a lesion-based sensitivity equal to 93.1%. This sensitivity performance was the result of classifying 20×20 pixels (patch resolution) rather than a pixel-resolution evaluation. Sinthanayothin's approach [10] could identify the exudates with 88.5% sensitivity and 99.7% specificity in terms of lesion-based accuracy against a small dataset comprising 21 abnormal and 9 normal retinal images. The performances were measured in terms of 10×10 pixels (patch-resolution), and no image-based and pixel-resolution accuracies were reported. Niemeijer *et al.* [12] achieved a good pixel-resolution accuracy of 95.5% sensitivity and 86.0% specificity for identification of retinal exudates. However, no image-based assessment was reported. We found Walter *et al.*'s [11] to be the only work that reported its diagnostic accuracy in terms of both image-based and pixel-resolution criteria. This technique achieved a pixel-resolution accuracy of 92.8% sensitivity, 92.4% predictivity, and an image-based sensitivity of 100.0% with 88.6% specificity on a set of 30 retinal images. However, some types of errors, especially on the border of the segmented exudates, were ignored in these reported performances. For example, when a pixel not selected by the clinician as exudate was wrongly chosen by the algorithm, it was not considered as a FP if the pixel was next to a selected exudate pixel by the clinician.

In terms of pixel resolution, our best results are 93.5% sensitivity and 92.1% predictivity that are slightly better than those in [11]. On the other hand, we could achieve a higher specificity with 94.6% accuracy with a lower sensitivity equal to 96.0%, both in terms of image-based criterion. It is worth noting that we assess our proposed approaches on a larger dataset of retinal images including 75 abnormal and 75 normal in addition to the further 150 images that are used to train and test the classifiers. It is assumed in [10] and [11] that the retinal images do not contain cotton wool spots as both methods have been implemented for the gray-level images. In contrast, our color retinal images contain cotton wool spots, and as discussed before, we have included some appropriate feature descriptors in our feature vectors to discriminate these lesions from exudates.

In terms of computational speed, our exudate identification method takes, on average, 3 min for processing each image on

a Pentium IV (3.4-GHz PC). This timing can be improved upon through a more efficient implementation.

V. DISCUSSION AND CONCLUSION

In this paper, we explore methods toward the development of an automated computational-intelligent-based decision support system for the purpose of detecting and classifying exudate pathologies of DR.

Past works on exudates identification mainly relied on gray-level information, and were assessed in terms of either lesion-based or image-based diagnostic accuracies against an approximately small dataset of retinal images. The reported lesion-based measurement was often an approximation of the real diagnostic accuracy as it was evaluated in a patch-resolution basis. Thus, the accuracy was obtained on, for example, a 10×10 or 20×20 pixel patches rather than a single pixel. There are certain errors in the reported patch-resolution accuracies due to small area that some exudates can occupy. While in medical decision support systems such as ours, an accurate diagnostic accuracy assessment in terms of both pixel-resolution and image-based is essential.

Here, we locate exudates at pixel level in color retinal images. We evaluate the diagnostic accuracy of our method in terms of both pixel-resolution and image-based criteria. Robustness and accuracy in comparison to expert ophthalmologists have been evaluated on a large image dataset. Indeed, we take advantage of retinal pathology–anatomical parts color information toward our objectives, and show the improvement obtained over gray-level-based techniques. The high performance of the proposed method is in part enabled by the integration of several efficient computational-intelligence-based methods, especially FCM color segmentation, GAs-based feature selection, and NN classifiers. Another important aspect of this study is that it tackles the varying retinal color, which may be due to skin pigmentation and iris color. In fact, without some type of color normalization, the larger variation in the natural retinal pigmentation across the patient dataset can hinder discrimination of the relatively small variations between the different lesion types. Thus, we apply a color normalization method to make the images invariant with respect to the background pigmentation variation and the exudate color variation between individuals.

The study presented here has shown encouraging results, and indicates that automated diagnosis of exudative retinopathy using combination of computational intelligence techniques and color retinal image analysis is very successful in detecting exudates. Hence, the system can be used to evaluate digital retinal images obtained in screening programmes for DR and used by nonexperts to indicate which patients require referral to an ophthalmologist for further investigation and treatment. We have shown that we can detect the large majority of exudates, and also most of our normal images can be correctly identified by the proposed system. This provides a huge amount of savings in terms of the number of retinal images that require to be manually reviewed by the medical professionals.

However, as this is an ongoing research, further development can be considered in the following two directions.

- 1) The first direction will be to establish the spatial relationship between the detected exudates and central macular area (fovea). This is because exudates and edema occurring more than 500 μm from the fovea, do not necessarily need treatment with the laser because they are not immediately sight-threatening, and may disappear spontaneously. To do this, we can build on our previous work of accurately locating the position of the optic disc.
- 2) Those automated systems that identify the presence of red lesions such as haemorrhages and microaneurysms are detecting the *earliest signs of DR* rather than *retinopathy requiring treatment*. We, however, anticipate that there will be a demand for a system that detect DR in its earliest stages as well as a system to detect exudates *requiring imminent treatment*. Thus, it will be useful to expand the present study by developing a system capable of detecting red lesions as well.

REFERENCES

- [1] R. Klein, B. Klein, S. Moss, M. Davis, and D. Demets, "The Wisconsin epidemiologic study of diabetic retinopathy II. Prevalence and risk of diabetic retinopathy when age at diagnosis is less than 30 years," *Arch. Ophthalmol.*, vol. 102, no. 4, pp. 520–526, 1984.
- [2] S. C. Lee, E. T. Lee, Y. Wang, and R. Klein, "Computer classification of nonproliferative diabetic retinopathy," *Arch. Ophthalmol.*, vol. 123, no. 6, pp. 759–764, 2005.
- [3] I. Ghafour, D. Allan, and W. Foulds, "Common causes of blindness and visual handicap in the west of Scotland," *Brit. J. Ophthalmol.*, vol. 67, no. 4, pp. 209–213, 1983.
- [4] R. Phillips, T. Spencer, P. Ross, P. Sharp, and J. Forrester, "Quantification of diabetic maculopathy by digital imaging of the fundus," *Eye*, vol. 5, pp. 130–137, 1991.
- [5] R. Phillips, J. Forrester, and P. Sharp, "Automated detection and quantification of retinal exudates," *Graefes Arch. Clin. Exp. Ophthalmol.*, vol. 231, pp. 90–94, 1993.
- [6] B. Ege, O. Larsen, and O. Hejlesen, "Detection of abnormalities in retinal images using digital image analysis," in *Proc. 11th Scand. Conf. Image Process.*, 1999, pp. 833–840.
- [7] H. Wang, H. Hsu, K. Goh, and M. Lee, "An effective approach to detect lesions in retinal images," in *Proc. IEEE Conf. Comput. Vis. Pattern Recogn.*, Hilton Head Island, SC, 2000, vol. 2, pp. 181–187.
- [8] G. Gardner, D. Keating, T. Williamson, and A. Elliott, "Automatic detection of diabetic retinopathy using an artificial neural network: A screening tool," *Brit. J. Ophthalmol.*, vol. 80, pp. 940–944, 1996.
- [9] A. Hunter, J. Lowell, J. Owens, and L. Kennedy, "Quantification of diabetic retinopathy using neural networks and sensitivity analysis," in *Proc. Artif. Neural Netw. Med. Biol.*, 2000, pp. 81–86.
- [10] C. Sinthanayothin, "Image analysis for automatic diagnosis of diabetic retinopathy," Ph.D. dissertation, King's College of London, London, U.K., 1999.
- [11] T. Walter, J. Klein, P. Massin, and A. Erginay, "A contribution of image processing to the diagnosis of diabetic retinopathy, detection of exudates in colour fundus images of the human retina," *IEEE Trans. Med. Imag.*, vol. 21, no. 10, pp. 1236–1243, Oct. 2002.
- [12] M. Niemeijer, B. V. Ginneken, S. R. Russell, M. Suttorp, and M. D. Abramoff, "Automated detection and differentiation of drusen, exudates and cotton-wool spots in digital color fundus photographs for diabetic retinopathy diagnosis," *Invest. Ophthalmol. Vis. Sci.*, vol. 48, pp. 2260–2267, 2007.
- [13] M. Goldbaum, S. Moezzi, A. Taylor, and S. Chatterjee, "Automated diagnosis and image understanding with object extraction, object classification and inferencing in retinal images," in *Proc. IEEE Int. Conf. Image Process.*, Lausanne, Switzerland, Sep. 16–19, 1996, vol. 3, pp. 695–698.
- [14] A. Osareh, B. Shadgar, and R. Markham, "Comparative pixel-level exudate recognition in color retinal images," in *International Conference on Image Analysis and Recognition (LNCS, vol. 3656)*, M. Kamel and A. Campilho, Eds. Toronto, Canada: Springer-Verlag, 2005, pp. 894–902.
- [15] R. Gonzalez and R. Woods, *Digital Image Processing*. Reading, MA: Addison-Wesley, 1992.
- [16] Y. Lim and S. Lee, "On the color image segmentation algorithm based on the thresholding and the fuzzy c-means techniques," *Pattern Recogn.*, vol. 23, no. 9, pp. 935–952, 1990.
- [17] K. Fukunaga, *Statistical Pattern Recognition*. New York: Academic, 1990.
- [18] S. Sangwine and R. Horne, *The Color Image Processing Handbook*. London, U.K.: Chapman and Hall, 1998.
- [19] A. Witkin, "Scale space filtering," in *Proc. Int. Joint Conf. Artif. Intell.*, 1983, pp. 1019–1022.
- [20] R. Krishnapuram and J. Keller, "A probabilistic approach to clustering," *IEEE Trans. Fuzzy Syst.*, vol. 1, no. 2, pp. 98–110, May 1993.
- [21] J. Dougman, "High confidence visual recognition of persons by a test of statistical independence," *IEEE Trans. Pattern Anal. Mach. Intell.*, vol. 15, no. 11, pp. 1148–1161, Nov. 1993.
- [22] J. Anil, N. Ratha, and S. Lakshmanan, "Object detection using Gabor filters," *Pattern Recogn.*, vol. 30, no. 2, pp. 295–309, 1997.
- [23] P. Moreno, A. Bernardino, and J. Santos, "Gabor parameter selection for local feature detection," in *Proc. 2nd Iberian Conf. Pattern Recogn. Image Anal.-IBPRIA*, 2005, pp. 11–19.
- [24] A. Drimbarean and P. F. Whelan, "Experiments in color texture analysis," *Pattern Recogn. Lett.*, vol. 22, no. 10, pp. 1161–1167, 2001.
- [25] O. Nestares, R. Navarro, J. Portilla, and A. Taberner, "Efficient spatial-domain implementation of a multiscale image representation based on Gabor functions," *J. Electron. Imag.*, vol. 7, no. 1, pp. 166–173, 1998.
- [26] B. Verma and P. Zhang, "A novel neural-genetic algorithm to find the most significant combination of features in digital mammograms," *Appl. Soft Comput.*, vol. 7, pp. 612–625, 2007.
- [27] G. Dijkstra, M. Hulle, and M. Wevers, "Genetic algorithm for feature subset selection with exploitation of feature correlations from continuous wavelet transform: A real case application," *Int. J. Comput. Intell.*, vol. 1, no. 1, pp. 1–12, 2004.
- [28] C. Bishop, *Neural Networks for Pattern Recognition*. London, U.K.: Oxford Univ. Press, 1995.
- [29] A. Osareh, M. Mirmehdi, B. Thomas, and R. Markham, "Comparison of color spaces for optic disc localization in retinal images," in *Proc. 16th Int. Conf. Pattern Recogn.*, 2002, pp. 743–746.



Alireza Osareh received the M.Sc. degree in artificial intelligence and robotics from Shiraz University, Shiraz, Fars, Iran, in 1997 and the Ph.D. degree in computer science from Bristol University, Bristol, U.K., in 2004.

He is currently an Associate Professor in Computer Science Department, Shahid Chamran University, Ahvaz, Iran. His current research interests include medical and biomedical engineering, biomedical informatics, machine learning, and pattern recognition.

Bitu Shadgar received the M.Sc. degree in software engineering from Ferdowsi University, Mashhad, Iran, in 1999 and the Ph.D. degree in computer science from Bristol University, Bristol, U.K., in 2003.

She is currently an Assistant Professor in Computer Science Department, Shahid Chamran University, Ahvaz, Iran. Her current research interests include Software engineering, databases, semantic web, and image annotation.

Richard Markham, photograph and biography not available at the time of publication.